Astronomy & Astrophysics manuscript no. hessj1825II
February 5, 2008
© ESO 2008

arXiv:astro-ph/0607548v1 24 Jul 2006

Energy dependent γ-ray morphology in the Pulsar wind nebula HESS J1825–137

F. Aharonian[1], A.G. Akhperjanian[2], A.R. Bazer-Bachi[3], M. Beilicke[4], W. Benbow[1], D. Berge[1], K. Bernlöhr[1,5], C. Boisson[6], O. Bolz[1], V. Borrel[3], I. Braun[1], A.M. Brown[7], R. Bühler[1], I. Büsching[8], S. Carrigan[1], P.M. Chadwick[7], L.-M. Chounet[9], R. Cornils[4], L. Costamante[1,22], B. Degrange[9], H.J. Dickinson[7], A. Djannati-Ataï[10], L.O'C. Drury[11], G. Dubus[9], K. Egberts[1], D. Emmanoulopoulos[12], P. Espigat[10], F. Feinstein[13], E. Ferrero[12], A. Fiasson[13], G. Fontaine[9], Seb. Funk[5], S. Funk[1], M. Füßling[5], Y.A. Gallant[13], B. Giebels[9], J.F. Glicenstein[14], P. Goret[14], C. Hadjichristidis[7], D. Hauser[1], M. Hauser[12], G. Heinzelmann[4], G. Henri[15], G. Hermann[1], J.A. Hinton[1,12], A. Hoffmann[16], W. Hofmann[1], M. Holleran[8], D. Horns[16], A. Jacholkowska[13], O.C. de Jager[8], E. Kendziorra[16], B. Khélifi[9,1], Nu. Komin[13], A. Konopelko[5], K. Kosack[1], I.J. Latham[7], R. Le Gallou[7], A. Lemière[10], M. Lemoine-Goumard[9], T. Lohse[5], J.M. Martin[6], O. Martineau-Huynh[17], A. Marcowith[3], C. Masterson[1,22], G. Maurin[10], T.J.L. McComb[7], E. Moulin[13], M. de Naurois[17], D. Nedbal[18], S.J. Nolan[7], A. Noutsos[7], K.J. Orford[7], J.L. Osborne[7], M. Ouchrif[17,22], M. Panter[1], G. Pelletier[15], S. Pita[10], G. Pühlhofer[12], M. Punch[10], B.C. Raubenheimer[8], M. Raue[4], S.M. Rayner[7], A. Reimer[19], O. Reimer[19], J. Ripken[4], L. Rob[18], L. Rolland[14], G. Rowell[1], V. Sahakian[2], A. Santangelo[16], L. Saugé[15], S. Schlenker[5], R. Schlickeiser[19], R. Schröder[19], U. Schwanke[5], S. Schwarzburg[16], A. Shalchi[19], H. Sol[6], D. Spangler[7], F. Spanier[19], R. Steenkamp[20], C. Stegmann[21], G. Superina[9], J.-P. Tavernet[17], R. Terrier[10], C.G. Théoret[10], M. Tluczykont[9,22], C. van Eldik[1], G. Vasileiadis[13], C. Venter[8], P. Vincent[17], H.J. Völk[1], S.J. Wagner[12], and M. Ward[7]

(Affiliations can be found after the references)

Preprint online version: February 5, 2008

ABSTRACT

Aims. We present results from deep γ-ray observations of the Galactic pulsar wind nebula HESS J1825–137 performed with the H.E.S.S. array.
Methods. Detailed morphological and spatially resolved spectral studies reveal the very high-energy (VHE) γ-ray aspects of this object with unprecedented precision.
Results. We confirm previous results obtained in a survey of the Galactic Plane in 2004. The γ-ray emission extends asymmetrically to the south and south-west of the energetic pulsar PSR J1826–1334, that is thought to power the pulsar wind nebula. The differential γ-ray spectrum of the whole emission region is measured over more than two orders of magnitude, from 270 GeV to 35 TeV, and shows indications for a deviation from a pure power law. Spectra have also been determined for spatially separated regions of HESS J1825–137. The photon indices from a power-law fit in the different regions show a softening of the spectrum with increasing distance from the pulsar and therefore an energy dependent morphology.
Conclusions. This is the first time that an energy dependent morphology has been detected in the VHE γ-ray regime. The VHE γ-ray emission of HESS J1825–137 is phenomenologically discussed in the scenario where the γ-rays are produced by VHE electrons via Inverse Compton scattering. The high γ-ray luminosity of the source cannot be explained on the basis of constant spin-down power of the pulsar and requires higher injection power in past.

Key words. ISM: plerions – ISM: individual objects: PSR B1823–13, HESS J1825–137, G18.0–0.7 – gamma-rays: observations

1. Introduction

A growing number of extended objects that seem to be associated with energetic pulsars are detected in the Galactic Plane by their very high-energy (VHE, energy $E_\gamma \gtrsim$ 100 GeV) γ-ray emission. Latest results on this class of objects include emission from MSH–15–52 (HESS J1514–591) (Aharonian et al. 2005a) and Vela X (HESS J0835–455) (Aharonian et al. 2006a), and the two sources in the Kookaburra region (HESS J1420–607 and HESS J1418–609) as described in Aharonian et al. (2006b). If these associations are correct, then these objects are pulsar wind nebulae (PWN), objects generally thought to be powered by a relativistic particle outflow (electrons and positrons) from a central source. The central source – a pulsar – is a rapidly rotating neutron star generated in a supernova event. The relativistic wind of particles flows freely out until its pressure is bal-

Send offprint requests to: Stefan Funk (Stefan.Funk@mpi-hd.mpg.de)

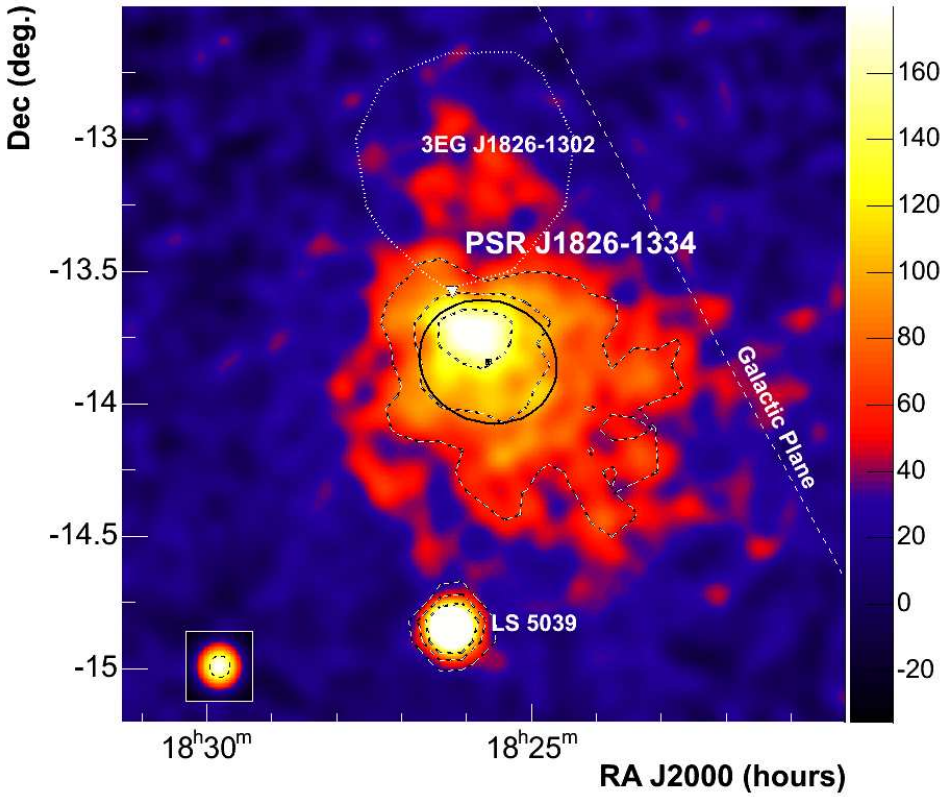

Fig. 1. Acceptance-corrected smoothed excess map (smoothing radius 2.5′) of the 2.7° × 2.7° field of view surrounding HESS J1825–137. The linear colour scale is in units of integrated excess counts within the smoothing radius of 2.5′. The excess has been derived from a model of the system acceptance as described in the text. The inset in the bottom left corner shows the PSF of the dataset (smoothed in the same way as the excess map with the black dashed circle denoting the smoothing radius). The dashed black and white contours are linearly spaced and denote the 5σ, 10σ and 15σ significance levels (the 5σ contour being the outermost one), determined with a $\theta = 0.1°$ radius cut. The best fit position of HESS J1825–137 is marked with a black square, the best extension and position angle by a black ellipse (see text). The dotted white contour shows the 95% positional confidence contour of the unidentified EGRET source 3EG J1826–1302. The position of the pulsar PSR J1826–1334 is marked by a white triangle. The bright point-source to the south of HESS J1825–137 is the microquasar LS 5039 (HESS J1826–148) (Aharonian et al. 2005d). The colour scale for this source is truncated in this Figure. The Galactic plane is shown as a white dashed line. Some indication for an additional emission region to the north of the pulsar is seen.

anced by that of the surrounding medium. In that region the wind decelerates and a standing termination shock is formed at which particles are accelerated (Kennel & Coroniti 1984a; Aharonian, Atoyan & Kifune 1997). The existence of electrons accelerated to energies > 100 TeV in such PWN has been established by X-ray observations of synchrotron emission, e.g. in the Crab nebula (Weisskopf et al. 2000). VHE γ-rays can be generated in PWN from the high-energy electrons by non-thermal bremsstrahlung or inverse Compton (IC) scattering on photon target fields, such as the cosmic microwave background (CMBR) or star-light photons.

One such object, HESS J1825–137, has been detected by the High Energy Stereoscopic System (H.E.S.S.) in a survey of the inner Galaxy (Aharonian et al. 2005b, 2006c) and has subsequently been associated with the X-ray PWN G18.0–0.7 surrounding the energetic pulsar PSR J1826–1334 (Aharonian et al. 2005c). This pulsar PSR J1826–1334 (also known as PSR B1823–13) was detected in the Jodrell Bank 20 cm radio survey (Clifton et al. 1992) and is among the 20 most energetic pulsars in the current ATNF catalogue (spin down power $\dot{E} = 3 \times 10^{36}$ erg/s). The distance of PSR J1826–1334 as measured from the dispersion of the radio pulses is 3.9 ± 0.4 kpc (Cordes & Lazio 2002). The radio detection further revealed characteristic properties of the system that are similar to those of the well studied Vela pulsar, namely a pulse period of 101 ms and a characteristic age of 21.4 kyears (derived by $\tau = P/2\dot{P}$). This age renders PSR J1826–1334 one of the 40 youngest pulsars detected so far (Manchester et al. 2005), and due to this, deep radio observations were performed to find emission associated with the remnant of the Supernova explosion that gave rise to the pulsar. However, deep VLA observations of the 20′ surrounding the pulsar have failed to detect this Supernova remnant (SNR) (Braun, Goss & Lyne 1989).

Initial observations of the region in X-rays with ROSAT (Finley et al. 1998) revealed a point source surrounded by an elongated diffuse region of size ∼5′. The X-ray emission region was subsequentially observed with the ASCA in-

strument and the data confirmed the picture of a compact object surrounded by an extended emission region (Sakurai et al. 2001). While ROSAT data did not provide sufficient statistics, ASCA data lacked the spatial resolution to resolve and interpret the sources in this region. The situation was clarified in an XMM-Newton observation in which high angular resolution observations revealed a compact core of extension 30″ surrounding PSR J1826–1334, and furthermore an asymmetric diffuse nebula extending at least 5′ to the south of the pulsar (Gaensler et al. 2003). In this XMM-Newton dataset the signal to noise ratio deteriorates rapidly at offsets larger than 5′ and for this reason the XMM data cannot place useful constraints on the presence of a faint shell of emission at larger radii as might be produced by an associated SNR. The extended asymmetric structure was attributed to synchrotron emission from the PWN of PSR J1826–1334 (Gaensler et al. 2003). The X-ray spectrum in the diffuse emission region follows a power law with photon index $\Gamma \sim 2.3$ and an X-ray luminosity between 0.5 and 10 keV of $L_x \sim 3 \times 10^{33}$ erg s^{-1} compared to the X-ray spectrum for the compact core following a power law with $\Gamma \sim 1.6$ and $L_x \sim 9 \times 10^{32}$ erg s^{-1} (these luminosities are derived assuming a distance of 4 kpc). Gaensler et al. (2003) discussed various scenarios to explain the asymmetry and offset morphology of the PWN G18.0–0.7. The most likely explanation seems to be that a symmetric expansion of the PWN is prevented by dense material to the north of the pulsar which shifts the whole emission to the south. Asymmetric reverse shock interactions of this kind have originally been proposed to explain the offset morphology of the Vela X PWN based on hydro-dynamical simulations by Blondin, Chevalier & Frierson (2001). Indeed recent analyses of CO data show dense material surrounding PSR J1826–1334 (at a distance of 4 kpc) to the north and north-east (Lemière et al. 2005), supporting this picture. It is interesting to note, that H.E.S.S. has now detected offset morphologies from both G18.0–0.7 and Vela X (Aharonian et al. 2006a), confirming the existence of a class of at least two offset PWN implied by X-ray observations (Gaensler et al. 2003). Whereas X-rays probe a combination of the thermal and ultrarelativistic components, which could have been mixed at the time when the asymmetric reverse shock interaction took place, the H.E.S.S. results are important in determining the offset morphology of the ultrarelativistic component alone.

Based on its proximity and energetics, the pulsar PSR J1826–1334 has been proposed to be associated with the unidentified EGRET source 3EG J1826–1302 (Hartman et al. 1999). This EGRET source exhibits a hard power law of photon index 2.0 ± 0.11 with no indication of a cut-off. The pulsar lies south of the centre of gravity of the EGRET position and is marginally enclosed in the 95% confidence contour (see Fig. 1). It has been shown (Zhang & Cheng 1998) that an association between PSR J1826–1334 and 3EG J1826–1302 is plausible based on the pulsar properties (such as pulsar period and magnetic field derived in the frame of an outer gap model), and that the observed γ-ray spectrum can be fit to this model. Although an unpulsed excess from EGRET has been reported with a significance of 9σ (Nel et al. 1996), a significant periodicity could not be established. Additionally an ASCA X-ray source possibly connected to the EGRET data above 1 GeV (Roberts, Romani & Kawai 2001) was found in this region. Recently, Nolan et al. (2003) reassessed the variability of the EGRET source and found a weak variability, which led the authors to consider the source finally as a PWN candidate in the EGRET high-energy γ-ray energy range above 100 MeV.

Here we report on re-observations of the VHE γ-ray source HESS J1825–137 and the region surrounding PSR J1826–1334 performed with H.E.S.S. in 2005. H.E.S.S. consists of four imaging atmospheric Cherenkov telescopes and detects the faint Cherenkov light from γ-ray induced air showers in the atmosphere above an energy threshold of 100 GeV up to several tens of TeV. Each telescope is equipped with a mirror area of 107 m^2 (Bernlöhr et al. 2003) and a 960 photo-multiplier camera for the detection of the faint Cherenkov light. The telescopes are operated in a coincidence mode in which at least two telescopes must have triggered in each event (Funk et al. 2004). The H.E.S.S. system has a point source sensitivity above 100 GeV of $< 2.0 \times 10^{-13}$ cm^{-2}s^{-1} (1% of the flux from the Crab nebula) for a 5σ detection in a 25 hour observation. The system is located in the Khomas Highland of Namibia (Hinton 2004) and began operation in December 2003.

2. H.E.S.S. observations of PSR J1826–1334

First indications of a VHE γ-ray signal in the region surrounding the pulsar PSR J1826–1334 during the H.E.S.S. Galactic plane survey (Aharonian et al. 2005b, 2006c) triggered pointed re-observations of the region, resulting in the detection of an 8.1σ significance signal – named HESS J1825–137 (Aharonian et al. 2005c). This significance was obtained using events within a circle of *a priori* chosen radius $\theta = 0.22^\circ$ from the best fit position as used in a blind search for somewhat extended sources. Using a larger integration radius of $\theta = 0.4^\circ$, appropriate to contain most of the emission region, the significance increased to 13.4σ. HESS J1825–137 was reported to extend $\sim 1^\circ$ asymmetrically to the south of PSR J1826–1334 and shows the same asymmetric extension as the X-ray PWN G 18.0–0.7 on a much larger scale. In Aharonian et al. (2005c) an association has been proposed between the H.E.S.S. source and the X-ray emission region. The different sizes in the two energy bands were explained by the difference in the synchrotron cooling lifetimes of the (higher energy) X-ray emitting and the (lower energy) IC-γ-ray emitting electrons. The energy spectrum of the source in the 2004 data within the larger integration circle of $\theta = 0.4^\circ$ was fitted by a power law of photon index $2.40 \pm 0.09_{\rm stat} \pm 0.2_{\rm sys}$ at a flux level corresponding to 20% of the flux from the Crab nebula above 1 TeV. The peak of HESS J1825–137 is located just outside the 95% confidence limits on the position of the unidentified EGRET source 3EG J1826–1302. As shown by Aharonian et al. (2005c), the H.E.S.S. energy spectrum can be connected to the EGRET spectrum by extrapolation. Therefore, despite the somewhat marginal spatial coincidence, an association between these two objects was considered.

HESS J1825–137 was revisited in 2005 for ~ 7 hours in pointed observations between June and July and was additionally in the field of view of a large part of the pointed observations on the nearby (distance $\sim 1^\circ$) γ-ray emitting mi-

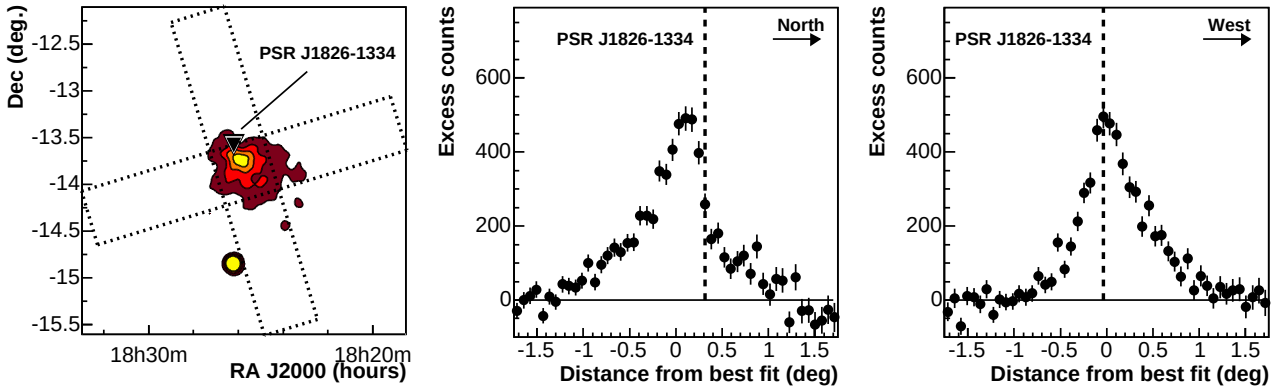

Fig. 2. Slices in the uncorrelated excess map of HESS J1825–137 to further illustrate the morphology. The width of the slices is 0.6° .The direction is given by the orientation from the fit of an elongated Gaussian (see Fig. 1) and has a value of 17° (central panel) and perpendicular to this direction (right panel). The left panel shows the region in which the slices were taken as black boxes overlaid on the H.E.S.S. excess map as shown in Fig. 1. The colors denote the 20%, 40%, 60% and 80% intensity contours of the VHE γ-ray emission. The slices are centred on the best fit position, the position of the pulsar in the slices is marked as a dashed black line. As a large part of the observations are taken south of HESS J1825–137, the range beyond 1° north of the pulsar is at the edge of the field of view of most observations, and the background subtraction is less reliable in this region.

croquasar LS 5039 (HESS J1826–146), adding another 50.9 hours between April and September (Aharonian et al. 2005d). Here we report on the total available dataset (i.e. 2004 and 2005 data) that includes now ∼67 hours of observations with HESS J1825–137 within 2.0° of the pointing position of the telescopes. The exposure adds up to a total dead-time corrected lifetime of 52.1 hours after quality selection of runs according to hardware and weather conditions, thereby increasing the observation time by more than a factor of 6 compared to earlier publications. The mean zenith angle of the dataset presented here is 20.1°, the mean offset of the peak position of HESS J1825–137 from the pointing direction of the system is 1.2°.

The standard H.E.S.S. event reconstruction scheme was applied to the raw data after calibration and tail-cuts cleaning of the camera images (Aharonian et al. 2004a). The shower geometry was reconstructed based on the intersection of the image axes, providing an angular resolution of ∼0.1° for individual γ-rays. Cuts on scaled width and length of the image (optimised on γ-ray simulations and off-source data) are applied to select γ-ray candidates and suppress the hadronic background (Aharonian et al. 2004b). The energy of the γ-ray is estimated from the total image intensity taking into account the shower geometry. The resulting energy resolution is ∼15%. As previously described (Aharonian et al. 2005b, 2006d), two sets of quality cuts are applied. For morphological studies of a source a rather tight image size cut of 200 photo-electrons (p.e.) is applied (along with a slightly tighter cut on the mean scaled width), yielding a maximum signal-to-noise ratio for a hard-spectrum source. For spectral studies the image size cut is loosened to 80 p.e. to extend the energy spectra to lower energies. Different methods are applied to derive a background estimate as described by Hinton, Berge & Funk (2005). For morphological studies the background at each test position in the sky is either derived from a ring surrounding this test position (with radius 1.0°, an area 7 times that of the on-source area, taking into account the changing acceptance on the ring), or from a model of the system acceptance, derived from off-data (data with no γ-ray source in the field of view) with similar zenith angle. In all background methods, known γ-ray emitting regions are excluded from the background regions to avoid γ-ray contamination of the background estimate. All results presented here have been obtained consistently with different background estimation techniques.

3. VHE γ-ray emission from HESS J1825–137

To illustrate the overall morphology of HESS J1825–137, Fig. 1 shows a smoothed excess map of the field of view surrounding the source, corrected for the changing relative acceptance in the field of view. The background for this map has been derived from a model of the system acceptance obtained from off-data (similar to the background estimation in Aharonian et al. (2006d)). The map has been smoothed with a Gaussian of width 2.5′. The inset in the bottom left corner shows a Monte-Carlo simulated point-source as it would appear in the same dataset taking the smoothing and the point-spread function (PSF) for this dataset into account. The pulsar PSR J1826–1334 is marked by a white triangle. To the south of HESS J1825–137, another VHE γ-ray source, the point-source microquasar LS 5039 (HESS J1826–148), is visible (Aharonian et al. 2005d). The color scale for this latter source is truncated and thus its apparent size is exaggerated. Also shown in Fig. 1 is the 95% positional confidence contour of the unidentified EGRET source 3EG J1826–1302 (dotted white), that is possibly associated to HESS J1825–137.

HESS J1825–137 shows a clearly extended morphology with respect to the PSF, extending to the south-west of the pulsar. The position and extension of HESS J1825–137 have been determined by fitting the uncorrelated (i.e. unsmoothed) excess map to a model of a 2-D Gaussian γ-ray brightness profile of the form $\rho \propto \exp(-\theta^2/2\sigma^2_{\rm source})$, convolved with the PSF for

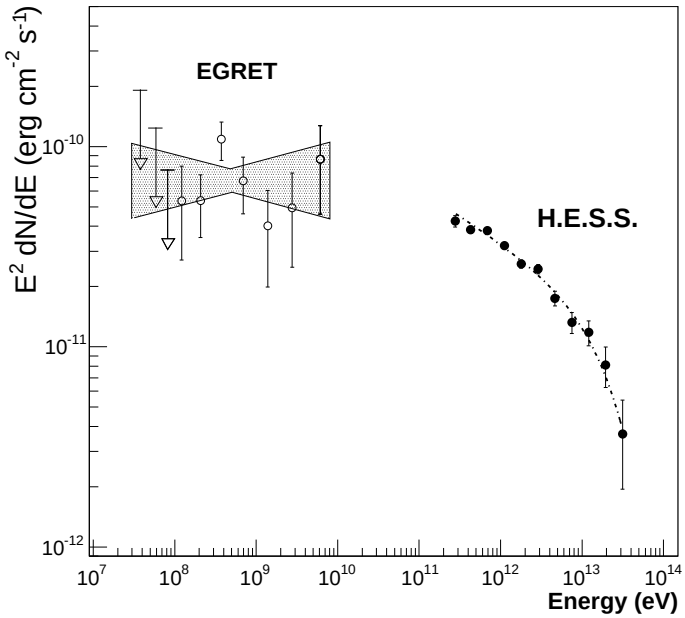

Fig. 3. Energy flux E^2dN/dE of HESS J1825–137 in γ-rays as measured by H.E.S.S. (black filled circles) up to ∼35 TeV for a large part of the emission region within an integration radius of 0.8° around the best fit position. Also shown as open circles are the energy flux points of the possibly related unidentified EGRET source 3EG J1826–1302. The background estimate for the spectrum has been derived from off-runs (i.e. runs without γ-rays in the field of view). The spectrum can be fit by a power law $dN/dE = I_0\, E^{-\Gamma}$ but the poor χ^2 of the fit (40.4 for 15 degrees of freedom) suggests a different spectral shape. Here a power law fit with an exponential cutoff is shown, but it should be noted that this shape is not favoured over other similarly complex spectral shapes as discussed in the text in more detail.

this dataset (68% containment radius: 0.075°). The best fit position – equivalent to the center of gravity of the source – is at 18h25m41s $\pm 3_{\rm stat}$s , –13°50′21″$\pm 35_{\rm stat}$″(here and in the following the epoch J2000 is used), the best fit rms extension is $\sigma_{\rm source} = 0.24^\circ \pm 0.02_{\rm stat}{}^\circ$. However, the χ^2 per degree of freedom is not satisfactory (1295/1085), indicative of the more complex morphology of the source. Reflecting the non-Gaussian and skewed source profile, the position of the peak in the γ-ray emission (at 18h25m57s, –13°43′36.8″as determined by fitting a 2-D Gaussian in a restricted region around the peak) is slightly shifted at a distance of ∼8′ to the best fit position. The pulsar PSR J1826–1334 is located at a distance of ∼10′ from the peak γ-ray emission and ∼17′ from the best fit position. To test for a different source morphology, an elongated Gaussian with independent $\sigma_{\rm source}$ along the minor and $\sigma'_{\rm source}$ along the major axis and a free position angle ω (measured counter-clockwise from the North) has also been fitted. This elongated fit gives a best fit position of 18h25m41s $\pm 4_{\rm stat}$s, –13°50′20″$\pm 40_{\rm stat}$″, consistent within errors to the symmetrical fit. The fit yields only a slight indication for an elongation with $\sigma_{\rm source} = 0.23 \pm 0.02_{\rm stat}$ and $\sigma'_{\rm source} = 0.26 \pm 0.02_{\rm stat}$ at a position angle of $\omega = 17^\circ \pm 12^\circ{}_{\rm stat}$. The χ^2 per degree of freedom (1288/1083) is still relatively poor. The best fit position deviates slightly from the best fit position reported in earlier papers (Aharonian et al. 2005b, 2006c). The difference can mainly be attributed to the different fit range. The best fit parameters of the elliptical fit are shown as a black square and ellipse in Fig. 1. Note that the fitted position angle is consistent within errors with the orientation of the line connecting the pulsar position and the best fit position, which amounts to 23.1°.

Fig. 2 shows slices in the direction of the position angle (17°) of the elliptical fit (centre) and in the direction perpendicular to it (right). The width of the slices is chosen to be 0.6°, the slices are illustrated in the left panel as black dashed boxes. The position of the pulsar in the slices is marked as a dashed black line. It can be seen, that the peak of the H.E.S.S. emission is close to the pulsar position but slightly shifted as is also apparent from the two-dimensional excess plot. Also visible in the central panel is the rather sharp drop from the peak position towards the north-eastern direction and the longer tail to the south-western direction. Some indication for an additional excess to the north of HESS J1825–137 is seen in Fig. 1 and in the central panel of Fig. 2 at a distance of ∼0.7° from the pulsar position. Further investigation of this feature will have to await future data, in particular given that most current data were taken on positions south of the pulsar, with regions in the north near the edge of the field of view.

For the spectral analysis the image size cut is loosened to 80 p.e. to achieve a maximum coverage in energy. The resulting spectral analysis threshold for the dataset described here is 270 GeV. Events with reconstructed direction within an angle $\theta = 0.8^\circ$ of the source location are considered on-source. No correction for the γ-ray emission extending beyond this angular cut has been applied. Thus the flux level determined corresponds to the flux level of the source within the integration region and might be an underestimation of the flux from the

Table 1. Fit results for different spectral models for the whole emission region within an integration radius of 0.8° around the best fit position and the background derived from off-data. The differential flux normalisation I_0 is given in units of $10^{-12}\,\mathrm{cm}^{-2}\,\mathrm{s}^{-1}\,\mathrm{TeV}^{-1}$. E, E_B, and E_c are given in units of TeV. The last column gives the integrated flux above the spectral analysis threshold of 270 GeV in units of $10^{-11}\,\mathrm{cm}^{-2}\,\mathrm{s}^{-1}$. The power-law fit provides a rather poor description of the data. Thus fits of a power law with an exponential cutoff (row 2), a power law with an energy dependent photon index (row 3), and a broken power law (row 4; in the formula, the parameter $S = 0.1$ describes the sharpness of the transition from Γ_1 to Γ_2 and is fixed in the fit) are also given. Note that some of the fit parameters are highly correlated.

Fit Formula for $\frac{\mathrm{d}N}{\mathrm{d}E}$	Fit Parameters				χ^2 (ndf)	$\mathrm{Flux}_{>270\ \mathrm{GeV}}$
$I_0\,E^{-\Gamma}$	$I_0 = 19.8 \pm 0.4$	$\Gamma = 2.38 \pm 0.02$			40.4 (15)	87.4 ± 2.0
$I_0\,E^{-\Gamma}\,\exp(-E/E_\mathrm{c})$	$I_0 = 21.0 \pm 0.5$	$\Gamma = 2.26 \pm 0.03$	$E_\mathrm{c} = 24.8 \pm 7.2$		16.9 (14)	86.7 ± 2.5
$I_0\,E^{-\Gamma+\beta\,\log E}$	$I_0 = 21.0 \pm 0.4$	$\Gamma = 2.29 \pm 0.02$	$\beta = -0.17 \pm 0.04$		14.5 (14)	82.8 ± 2.2
$I_0\,(E/E_\mathrm{B})^{-\Gamma_1}\left(1+(E/E_\mathrm{B})^{1/S}\right)^{S\,(\Gamma_1-\Gamma_2)}$	$I_0 = 2.2 \pm 1.0$	$\Gamma_1 = 2.26 \pm 0.03$	$\Gamma_2 = 2.63 \pm 0.07$	$E_\mathrm{B} = 2.7 \pm 0.5$	15.1 (13)	84.6 ± 38.5

whole source. In the determination of the energy spectrum, the energy of each event is corrected for the time-varying detector optical efficiency, relative to that used in Monte Carlo simulations to estimate the effective area of the instrument. The optical efficiency is estimated from single muon events detected during each observation run (Leroy et al. 2003; Bolz 2004). The mean energy correction is ∼25%. For the spectral analysis the background is taken from positions in the same field of view with the same offset from the pointing direction as the source region. This approach is taken to avoid systematic effects from the energy-dependent system acceptance function (which is to a good approximation radially symmetric). In another approach off-data have been used in the background estimation to confirm the results from the same field of view, using either the same shaped region as the on-region in the off-data or using again off-regions distributed with the same offset from the pointing direction of the system as the on-region. The total significance of the emission region with the loose cuts is 33.8σ with an excess of 19510 ± 577 γ-ray events. Fig. 3 shows the spectral energy distribution in terms of energy flux E^2dN/dE of the H.E.S.S. emission region (full black circles). Also shown are the energy flux points and the spectral fits of the possibly related unidentified EGRET source 3EG J1826–1302 (open circles). Given the poor angular resolution of EGRET, these data are taken on a scale similar to that of the full H.E.S.S. emission region and can thus be compared to the total H.E.S.S. flux. From this figure one can see that the unidentified EGRET source 3EG J1826–1302 could be associated with the H.E.S.S. emission region from a spectral continuity point of view.

A fit of the differential energy spectrum from 270 GeV up to ∼35 TeV by a power law $dN/dE = I_0\,E^{-\Gamma}$ yields a normalisation of $I_0 = 19.8 \pm 0.4_\mathrm{stat} \pm 4.0_\mathrm{sys} \times 10^{-12}$ TeV^{-1} cm^{-2} s^{-1} and a photon index $\Gamma = 2.38 \pm 0.02_\mathrm{stat} \pm 0.15_\mathrm{sys}$ (see Table 1). The flux of HESS J1825–137 above 1 TeV corresponds to ∼68% of the flux from the Crab nebula. Note that this flux is significantly higher than the previously reported flux (Aharonian et al. 2005c) due to a significantly increased integration radius (0.8° instead of 0.4°) in the attempt to cover the whole source region. Integrating only within the smaller region of 0.4° the flux level is consistent with the previously published result. The power-law fit represents a rather bad description of the data (as can be seen χ^2 of the fit) and suggests therefore a different spectral shape. Various models have been fit to the data to investigate the shape of the spectrum. Table 1 summarises these fits. Three alternative shapes have been used: a power law with an exponential cutoff E_c (row 2), a power law with an energy dependent exponent (row 3), and and a broken power law (row 4). In all cases, I_0 is the differential flux normalisation, and the photon indices are specified as Γ. It is evident that the alternative descriptions of the spectrum describe the data significantly better than the pure power law as can be seen from the decreasing χ^2/ndf (see Table 1).

Given the large dataset with more than 19,000 γ-ray excess events and given the extension of HESS J1825–137, a spatially resolved spectral analysis has been performed to search for a change in photon index across the source, similar to the detailed analysis of the γ-ray SNR RX J1713.7–3946 as performed in Aharonian et al. (2006d). Fig. 4 shows energy spectra determined in radial bins around the pulsar position, covering the extended tail of the VHE γ-ray source. The inset of Fig. 4 shows again the H.E.S.S. excess map as shown in Fig. 1 along with wedges that illustrate the regions in which the energy spectra were determined, with radii increasing in steps of 0.1°; the innermost region is centred on the pulsar PSR J1826–1334. The opening angle of the wedges was constrained by LS 5039 in the southern part and by the apparent end of the emission region in the northern part. For all regions the energy spectrum has been determined by defining the wedge as the on-region. The background estimate has been derived from circles distributed on a ring around the pointing direction. The radius of this ring was chosen to be equal to the distance of the centre of gravity of the wedge to the pointing direction. This approach ensures a similar offset distribution in the on- and off-dataset and has been used to determine the background estimate from the same field of view as well as from off-data taken on regions without γ-ray sources. Consistent results were achieved in both methods.

Along with each spectrum in Fig. 4, the power law fit to the innermost region centred on the pulsar position is shown as a dashed line for comparison. A softening of the energy spectra is apparent with increasing distance from the pulsar. This softening is equivalent to a decrease of the source size with increasing energy and provides the first evidence for an energy dependent morphology detected in VHE γ-rays. Differences in the energy bin sizes arise from the fact that for non-significant photon points the bin size was increased. It has been verified

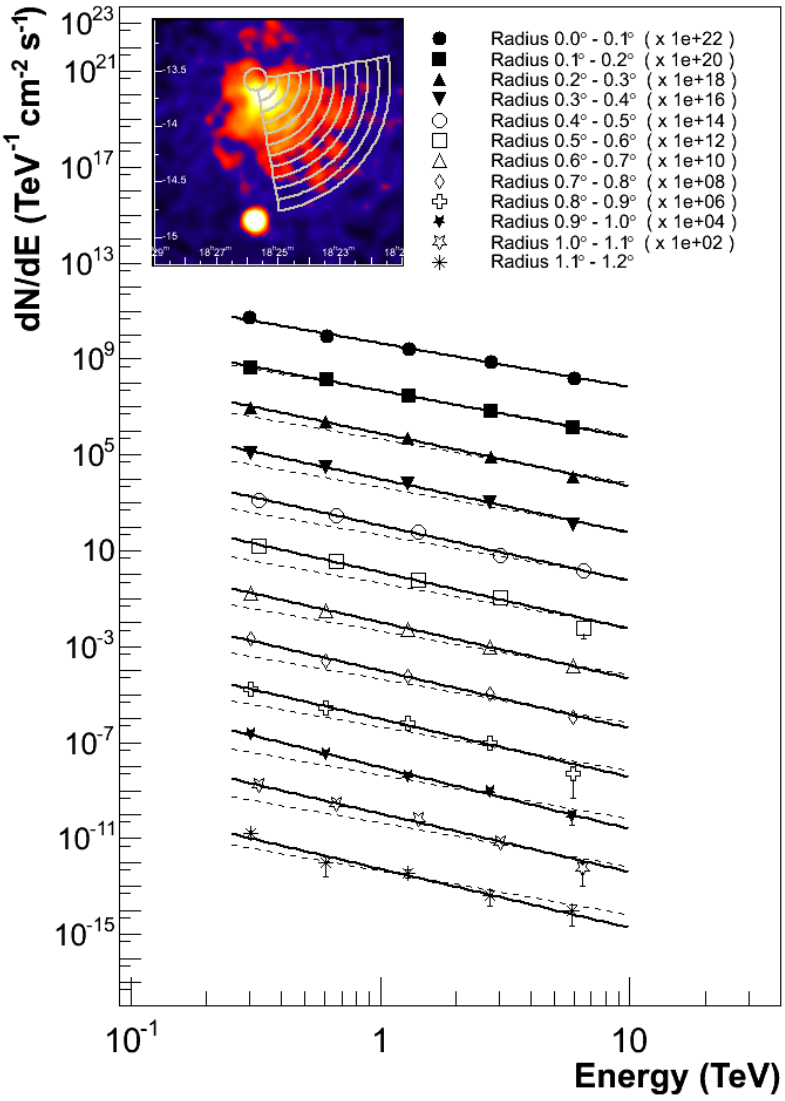

Fig. 4. Energy spectra in radial bins. **Inset:** H.E.S.S. excess map as shown in Fig. 1. The wedges show the radial regions with radii in steps of 0.1° in which the energy spectra were determined. The innermost region is centred on the pulsar PSR J1826–1334. **Main Figure:** Differential energy spectra for the regions illustrated in the inset, scaled by powers of 10 for the purpose of viewing. The spectrum for the analysis at the pulsar position is shown as a reference along with the other spectra as dashed line. For all regions the energy spectrum has been determined as described in the text and has been fitted by a power-law in a restricted energy range between 0.25 and 10 TeV.

that this approach does not change the result of the fit. Due to the different distribution of offsets from the pointing direction of the system in the different regions, the photon analysis threshold changes slightly, thus some of the different spectra do not start at exactly the same energy.

Fig. 5 summarises the findings of Fig. 4 by plotting the fit parameters of the power law fit versus the distance of the region to the pulsar position. Shown are the results using two different background estimation techniques in the spectral analysis. The left panel shows the photon index as a function of the distance from the pulsar. A clear increase of the photon index for larger distances from the pulsar position is apparent; the photon index seems to level off within errors to a value of ∼2.4 ±0.1 at a distance of ∼0.6°. The right panel shows the surface brightness (i.e. the integrated energy flux EdN/dE per unit area between 0.25 TeV and 10 TeV) as a function of the distance to the pulsar position. Again here it can be seen, that the maximum of the emission is slightly shifted away from the pulsar position as was already apparent in Fig. 2. In both panels, the error bars denote $\pm 1\sigma$ statistical errors. Systematic errors of 20% on the flux and 0.15 on the photon index are to be assigned to each data point in addition. However, since all spectra come from the same set of observations, these systematic errors should be strongly correlated, and will cancel to a large extent when different wedges are compared. Table 2 summarises the different spectral parameters determined in the wedges using the reflected background from the same field of view.

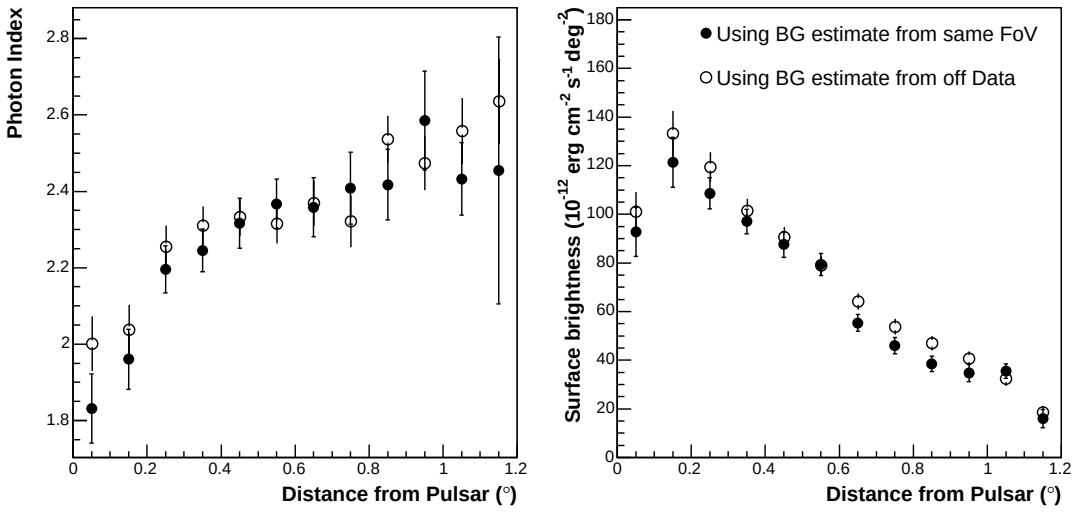

Fig. 5. Energy spectra in radial bins. **Left:** Power-law photon index as a function of the radius of the region (with respect to the pulsar position) for the regions given in Fig. 4. The closed points are obtained by deriving the background estimate from regions with the same offset as the on-region within the same field of view. The open points are derived using off-data (data without γ-ray sources in the field of view) for the background estimate. A constant fit to the filled points yields a χ^2 of 58 for 11 degrees of freedom, clearly showing the dependence of the photon index on the distance from the pulsar position. **Right:** Surface brightness between 0.25 and 10 TeV per integration region area in units of 10^{-12}erg cm^{-2} s^{-1} deg^{-2} as a function of the distance to the pulsar position. Error bars denote $\pm 1\sigma$ statistical errors.

Table 2. Spectral parameters for the radial bins surrounding PSR J1826–1334. *PSF* denotes a H.E.S.S. point-source analysis at the pulsar position. The background estimate for the numbers in the table have been derived from reflected positions within the same field of view. The energy flux and surface brightness are given for the energy range between 0.25 and 10 TeV.

Radius (deg)	Photon Index	χ^2/ndf	Area (deg^2)	Energy Flux (erg cm^{-2} s^{-1})	Surface Brightness (erg cm^{-2} s^{-1} deg^{-2})
PSF	1.83 ± 0.09	2.8 / 3	3.1e-02	2.9e-12 ± 3.2e-13	9.3e-11 ± 1.0e-11
0.15	1.96 ± 0.08	0.8 / 3	2.4e-02	2.9e-12 ± 2.4e-13	1.2e-10 ± 1.0e-11
0.25	2.20 ± 0.06	3.1 / 3	3.9e-02	4.3e-12 ± 2.5e-13	1.1e-10 ± 6.4e-12
0.35	2.25 ± 0.06	6.9 / 3	5.5e-02	5.3e-12 ± 2.8e-13	9.7e-11 ± 5.1e-12
0.45	2.32 ± 0.07	7.1 / 3	7.1e-02	6.2e-12 ± 3.7e-13	8.8e-11 ± 5.2e-12
0.55	2.37 ± 0.06	8.5 / 3	8.6e-02	6.9e-12 ± 3.9e-13	7.9e-11 ± 4.5e-12
0.65	2.36 ± 0.08	0.4 / 3	1.0e-01	5.7e-12 ± 3.6e-13	5.5e-11 ± 3.5e-12
0.75	2.41 ± 0.09	8.3 / 3	1.2e-01	5.4e-12 ± 4.0e-13	4.6e-11 ± 3.4e-12
0.85	2.42 ± 0.09	6.0 / 3	1.3e-01	5.1e-12 ± 4.2e-13	3.8e-11 ± 3.1e-12
0.95	2.59 ± 0.13	2.4 / 3	1.5e-01	5.2e-12 ± 5.4e-13	3.5e-11 ± 3.6e-12
1.05	2.43 ± 0.09	6.4 / 3	1.6e-01	5.9e-12 ± 4.9e-13	3.6e-11 ± 3.0e-12
1.15	2.45 ± 0.35	3.4 / 3	1.8e-01	2.9e-12 ± 6.8e-13	1.6e-11 ± 3.8e-12

Whereas the H.E.S.S. observation of an energy dependent morphology represents the first detection of such an effect in γ-ray astronomy, the dependence of observed photon index on radius (commonly known as "$\Gamma - r$" relation) is well known from X-ray observations of PWN other than the Crab. For G21.5–0.9 Slane et al. (2000) found a value of $\Gamma \sim 1.5$ near the PWN termination shock, after which it converges to a value of ∼2.2 in the outer nebula. For the PWN 3C58, the photon index increases from 1.9 in the torus to ∼2.5 at the edge of 3C58 (Slane et al. 2004). For this object Bocchino et al. (2001), also found that the energy flux per radial interval for 3C58 remains approximately constant, consistent with our findings for HESS J1825–137. A similar constant energy flux with increasing radius was also found in X-ray observations of another VHE γ-ray source G0.9+0.1 (Porquet, Decourchelle & Warwick 2003). For this composite remnant, the photon index also varies with radius from 1.5 (beyond the compact core) to ∼2.5 near the edge of the PWN. In the case of the more evolved Vela PWN Mangano et al. (2005) found a radial variation of 1.55 to 2.0. For most of these remnants a total change in the photon index of ∼0.5 is seen, as expected for cooling losses. Attempts to model the $\Gamma - r$ relationship were not successful in the past – Slane et al. (2004) showed that the Kennel & Coroniti (1984b) model for convective flow (which includes the conservation of magnetic flux) fails to reproduce this well-known $\Gamma - r$ relationship for PWN which are evolved beyond the Crab phase. It should additionally be noted, that the H.E.S.S. observation of

an energy dependent morphology is the first unambiguous detection of a spectral steepening away from the pulsar, for fixed electron energies; in X-rays the situation is complicated by a possible variation of the magnetic field with increasing distance from the pulsar; if the X-ray spectrum is probed near or above the peak of the SED, a variation of the field will influence the slope. Depending on the age and magnetic field, one might expects to see similar effects in other VHE γ-ray PWN, but so far only HESS J1825–137 has sufficient statistics to clearly reveal the energy dependent morphology.

To further investigate the spectral properties of HESS J1825–137, the emission region has been segmented into boxes. The result of the spectral analysis in these boxes is shown in Fig. 6. The left panel shows in red VHE γ-ray excess contours as given in Fig. 1. Overlaid are 12 boxes for which spectra were obtained independently. The photon index resulting from a power law fit in each region is grey-scale coded in bins of 0.1. Also here a softening of the spectral indices away from the pulsar position is apparent, although the error bars are larger than in Fig. 5 due to the smaller integration regions. The size of the boxes is equivalent to the ones used in the analysis of the shell-type SNR RX J1713.7–3946 (Aharonian et al. 2006d), where no spectral variation has been detected. The right hand figure shows the correlation of photon index Γ to integral flux per square degree above 1 TeV. A mild correlation between the flux per deg^2 and the spectral index exists and the correlation coefficient between these two quantities is -0.46 ± 0.14.

4. Interpretation

Obviously, the key aspect of the new H.E.S.S. data is the softening of the energy spectrum at larger distances from the pulsar position or equivalently, the decrease in source size with increasing energy of the γ-rays. The following discussion is based on the plausible assumption that particles have been accelerated in the proximity of the pulsar during the last 20 kyears – the characteristic age of the pulsar – and that they were then transported by diffusion and/or convection to form the extended nebula of about 10–15 pc radius (for a recent review of PWN see Gaensler & Slane 2006). The asymmetric shape of the nebula most likely reflects the ambient conditions, and could be caused by a reverse supernova shock created in the dense medium north of the pulsar (van der Swaluw & Wu 2001; Aharonian et al. 2005c), geometrically by the motion of the pulsar leaving a PWN 'trail', or even dynamically by a bow shock, resulting in a 'cometary' tail; however, the high speeds in excess of 1000 km/s required in case of HESS J1825–137 favour the first scenario. Spectral variation with distance from the pulsar could result from (i) energy loss of particles during propagation, with radiative cooling of electrons propagating outward from the pulsar termination shock as the obvious loss mechanism, as well as from (ii) energy dependent diffusion or convection speeds, and from (iii) variation of the shape of the injection spectrum with age of the pulsar which, after propagation, translates into a spatial variation of spectra.

Loss mechanisms in (i) include, e.g, adiabatic expansion, ionisation loss, bremsstrahlung, synchrotron losses and inverse Compton (IC) losses; only the last two result in a lifetime $\tau = E/(\mathrm{d}E/\mathrm{d}t)$ which decreases with energy and hence causes power-law spectra to steepen, due to the quadratic dependence of $\mathrm{d}E/\mathrm{d}t$ on the particle energy (Blumenthal & Gould 1970; Kardashev 1962). A source size which decreases with energy is therefore a strong indication that the accelerated particles are electrons. The lifetime due to synchrotron and IC losses is:

$$\tau_{\rm rad} \approx 3.1 \times 10^5 \left(\frac{w_r}{\rm eV\,cm^{-3}}\right)^{-1} \left(\frac{E_e}{\rm TeV}\right)^{-1} \ {\rm yr}. \quad (1)$$

Here, $w_r = \eta w_{\rm ph} + 0.025\,{\rm eVcm^{-3}}({\rm B}/\mu{\rm G})^2$ is the total energy density in the form of radiation and magnetic fields, η is a normalisation factor to account for the reduction of IC losses due to the transition into the Klein-Nishina regime and B the magnetic field. Given the density of the 2.7 K CMBR $w_{2.7{\rm K}} = 0.26$ eVcm^{-3}, and the fact that IC losses of multi-TeV electrons on the diffuse optical/IR photons are strongly suppressed due to the Klein-Nishina effect, and even for the CMBR are reduced by a factor $\eta \approx 2/3$ at H.E.S.S. energies, synchrotron losses dominate for $B > 3\ \mu$G. In case of continuous injection and radiative lifetimes short compared to the age of the source, $\tau_{\rm rad}(E) \ll T$, the spectral index α of the electrons steepens by one unit, corresponding to a change of the photon index by half a unit, which approximately matches the observed variation between the inner and outer regions of the nebula (Fig. 5). In the Thomson regime, the energy of the parent electrons is $E_e \approx 20(E_\gamma/{\rm TeV})^{1/2}$ TeV, corresponding to the range from about 10 to 100 TeV for γ-ray energies between 0.2 and 20 TeV. Cooling time scales below 20 kyears require $B > 6\ \mu$G for 10 TeV electrons; at 100 TeV the lifetime is below 20 kyears already in typical 3 μG interstellar fields, so some steepening of spectra at the highest energies is expected even in relatively modest fields.

It is then instructive to consider the energy budget of the PWN in an electronic scenario. The assumed large distance of $\approx$ 4 kpc and the relatively high γ-ray flux, $F \simeq 1.5 \times 10^{-10}$ erg/cm^{2}s above 200 GeV, imply a quite luminous VHE γ-ray source, $L_\gamma \sim 3 \times 10^{35}$ erg/s. This luminosity is comparable to that of the Crab nebula, while the spin-down luminosity of the pulsar is smaller by two orders of magnitude. Thus, the efficiency of the γ-ray production in HESS J1825–137 is much higher, $\epsilon_\gamma = L_\gamma(>200{\rm GeV})/{\rm L_{rot}} \approx 0.1$. A relatively large efficiency is not unexpected (Aharonian, Atoyan & Kifune 1997) since the much lower magnetic field in a nebula powered by a less energetic pulsar results in a more favourable sharing between IC and synchrotron energy losses. In a steady state, and neglecting non-radiative energy losses, the efficiency for γ-ray production is

$$\epsilon_\gamma \approx \epsilon_e \frac{\tau_{\rm rad}}{\tau_{\rm IC}} \approx \epsilon_e \frac{\eta w_{\rm ph}}{\eta w_{\rm ph} + 0.025{\rm eVcm^{-3}}({\rm B}/\mu{\rm G})^2} \quad (2)$$

where $\tau_{\rm IC}$ is the lifetime due to IC losses and ϵ_e is the fraction of pulsar spin-down power going into 10 to 100 TeV electrons, corresponding to the observed γ-ray energies. Unless the electron spectral index is well below 2 at energies below 10 TeV, ϵ_e will be below 10-15%, taking into account the sharing of spin-down energy between particle and field energies. An efficiency ϵ_γ of 0.1 cannot be obtained, even for rather small magnetic

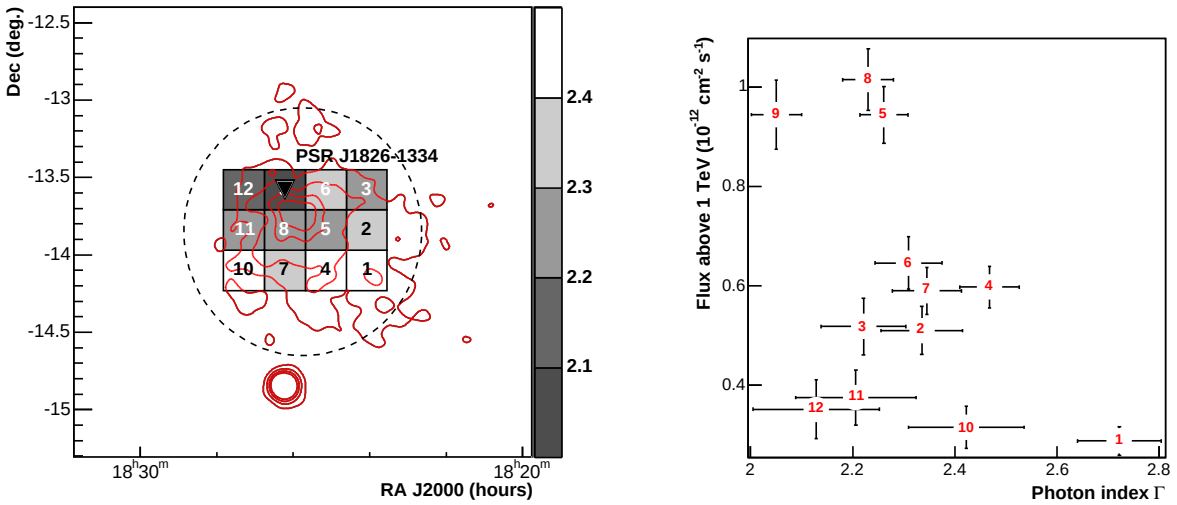

Fig. 6. Spatially resolved spectral analysis of HESS J1825–137. **Left:** Shown in solid red are VHE γ-ray excess contours from Fig. 1, linearly spaced at the 20%, 40%, 60% and 80% maximum intensity levels. Superimposed are the 12 boxes ($0.26^\circ \times 0.26^\circ$) for which spectra were obtained. The black dashed line is the 0.8° radius circle that was used to integrate events to produce a spectrum of the whole region. The photon index obtained from a power-law fit in each region is colour coded in bins of 0.1. **Right:** Integral flux above 1 TeV per square degree versus photon index, for the 12 regions shown in the left panel. The error bars are $\pm 1\sigma$ statistical errors. The correlation coefficient for the two quantities is -0.46 ± 0.14.

fields in the range of a few μG. Detailed numerical simulations with (optionally time-dependent) electron injection and cooling confirm that an energy input about one order of magnitude higher than the current spin-down luminosity is required to sustain the observed gamma-ray flux and to quantitatively reproduce the measured spectrum, assuming that the distance of ~ 4 kpc is correct. A likely solution is that the spin-down power of the pulsar was significantly higher in the past; for modest B fields of a few μG electron lifetimes in particular at lower energies are of the order of the pulsar age and the time variation of spin-down luminosity needs to be taken into account. For example, with $L_{\rm rot} \propto t^{-2}$ for a braking index of $n = 3$, 'relic' electrons released in the early history of the pulsar and surviving until today can provide sufficient energy. To allow accumulation of electrons over the history of the pulsar, magnetic fields should not exceed 10 μG.

A discussion of the energy-dependent morphology requires assumptions concerning the transport mechanism. At least in the inner regions of the nebula, convection is likely to dominate over diffusion. Indeed, the variation of surface brightness across the source – roughly proportional to $1/\theta$, where θ is the angular distance from the pulsar (see Table 2) – is difficult to account for in purely diffusive propagation. A surface brightness $\propto \theta^{-n}$ is obtained – for spherical symmetry – from a volume density $\propto r^{-n-1}$. Neglecting cooling effects, a $1/\theta$ dependence is hence obtained for a constant radial convection velocity, resulting in a $1/r^2$ density distribution. For constant convection speed, energy conservation requires a rapid decrease of B-fields with distance from the pulsar, with very low fields at the edge of the PWN unless one is dealing with a very strong and young source such as the Crab nebula (Kennel & Coroniti 1984b). A convection speed $v(r) \propto 1/r$ would allow a constant B-field. Such convection results in constant surface density; however, the electron density at a fixed electron energy – and therefore the γ-ray intensity – will again decrease with distance once cooling is included. A speed $v(r) \propto 1/r$ results in a propagation time $t \sim r^2$ and, at energies where the electron lifetime $\tau_{\rm rad} \propto 1/E_e$ is shorter than the lifetime T of the accelerator, in a source size $R \propto E_e^{-1/2}$.

A similar result is obtained for the diffusion case (ii), which is expected to be relevant near the outer edge of the nebula. The diffusive source size is governed by the diffusion coefficient $D(E)$, which is frequently parametrised in a power-law form $D(E) = D_0(E/E_0)^\delta$, with δ between 0 for energy-independent diffusion and 1 for Bohm diffusion. The resulting size can be estimated to $R \simeq [2D(E)t]^{1/2}$ with the propagation time t again given by the age T of the accelerator or the lifetime $\tau_{\rm rad}$ of radiating particles, whatever is smaller. For lifetimes $\tau_{\rm rad} \ll T$ short compared to the age of the accelerator, one obtains $R \propto E_e^{(\delta-1)/2}$. In case of Bohm-type diffusion with $\delta = 1$, the radiative losses and the diffusion effects compensate each other and the size becomes effectively energy independent. For energy independent diffusion, i.e. $\delta = 0$, the size decreases with energy again as $R \propto E_e^{-1/2}$.

Option (iii) - a time-variable acceleration spectrum - is a distinct possibility in particular for accelerated electrons. Higher pulsar spin-down luminosity in the past will have been associated with higher B fields and a lower cutoff energy, governed by the relation between acceleration and radiative cooling time scales. In either case (i), (ii) or (iii), the new H.E.S.S. results therefore provide evidence of an electronic origin of the VHE γ-ray emission, and require that characteristic cooling time scales are, or at some earlier time were, shorter than the age of the nebula.

4.1. Conclusion

We have presented detailed morphological and spectral studies of the VHE γ-ray source HESS J1825–137 that has been originally detected in the survey of the inner Galaxy, conducted by H.E.S.S. in 2004. The γ-ray spectrum of the source has been measured over more than two decades between ~270 GeV and ~35 TeV. The energy spectrum shows indications for a deviation from a pure power-law. Several spectral shapes have been applied to fit the data and it seems, that a broken power-law or a power-law with energy dependent photon index provide a better description than a pure power law. The large data set has provided the possibility for a spatially resolved spectral study. A significant softening of the γ-ray spectrum away from the position of the energetic pulsar PSR J1826–1334 has been found, providing the first direct evidence of an energy dependent morphology in VHE γ-rays. The studies performed here significantly strengthen the case that the VHE γ-ray emission originates in the wind nebula of PSR J1826–1334. It is difficult to explain the measured γ-ray luminosity in terms of the current spin-down luminosity of the pulsar. A like scenario is a significant contribution of 'relic' electrons released in the early history of the pulsar, when the spin-down luminosity is higher. The variation of index with distance from the pulsar is attributed both to IC and synchrotron cooling of the continuously accelerated electrons.

Acknowledgements. The support of the Namibian authorities and of the University of Namibia in facilitating the construction and operation of H.E.S.S. is gratefully acknowledged, as is the support by the German Ministry for Education and Research (BMBF), the Max Planck Society, the French Ministry for Research, the CNRS-IN2P3 and the Astroparticle Interdisciplinary Programme of the CNRS, the U.K. Particle Physics and Astronomy Research Council (PPARC), the IPNP of the Charles University, the South African Department of Science and Technology and National Research Foundation, and by the University of Namibia. We appreciate the excellent work of the technical support staff in Berlin, Durham, Hamburg, Heidelberg, Palaiseau, Paris, Saclay, and in Namibia in the construction and operation of the equipment.

References

Aharonian, F. A., Atoyan, A., & Kifune, T. 1997, MNRAS 291, 162
Aharonian, F. A., et al. (*H.E.S.S. Collaboration*) 2004a, APh 22, 109
Aharonian, F. A., et al. (*H.E.S.S. Collaboration*) 2004b, A&A 430, 865
Aharonian, F. A., et al. (*H.E.S.S. Collaboration*) 2005a, A&A 435, L17
Aharonian, F. A., et al. (*H.E.S.S. Collaboration*) 2005b, Science 307, 1938
Aharonian, F. A., et al. (*H.E.S.S. Collaboration*) 2005c, A&A 442, L25
Aharonian, F. A., et al. (*H.E.S.S. Collaboration*) 2005d, Science 309, 746
Aharonian, F. A., et al. (*H.E.S.S. Collaboration*) 2006a, A&A, 448, L43
Aharonian, F. A., et al. (*H.E.S.S. Collaboration*) 2006b, in press (astro-ph/0606311)
Aharonian, F. A., et al. (*H.E.S.S. Collaboration*) 2006c, ApJ 636, 777
Aharonian, F. A., et al. (*H.E.S.S. Collaboration*) 2006d, A&A 449, 223
Bernlöhr, K. et al. 2003, APh 20, 111
Blondin, J.M., Chevalier, R.A., & Frierson, D.M. 2001, ApJ 563, 806
Blumenthal, G. R., Gould, R. J. 1970, Rev. Mod. Phys 42, 237
Bocchino, F., Warwick, R. S., Marty, P., Lumb, S., Becker, W., & Pigot, C. 2001, A&A 369, 1078
Bolz, O. 2004, PhD thesis, Karl-Ruprecht University Heidelberg (http://www.ub.uni-heidelberg.de/archiv/4812)
Braun, R., Goss, W. M., & Lyne, A. G., 1989, ApJ 340, 355
Clifton, T. R., Lyne, A. G., Jones, A. W., McKenna, J., & Ashworth, M. 1992, MNRAS 254, 177
Cordes, J. M., & Lazio, T. J. W. 2002, preprint (astro-ph/0207156)
Finley, J. P., Srinivasan, R., & Park, S. 1996, ApJ 466, 938
Funk, S. et al. 2004, APh 22, 285
Gaensler, B. M., Schulz, N. S., Kaspi, V. M. Pivovaroff, M. J., & Becker, W. E. 2003, ApJ 588, 441
Gaensler, B. M., & Slane, P. O. 2006, To appear in Annual Review of A&A. (astro-ph/0601081)
Hartman, R. C., et al., 1999, ApJS 123, 79
Hinton, J. A. 2004, NewAR 48, 331
Hinton, J. A., Berge, D., & Funk, S. 2005, Proc. of Towards a Network of Atmospheric Cherenkov Detectors VII (Palaiseau), 183
Kardashev, N. S. 1962, Sov. Astr. 6, 317
Kennel, C. F., Coroniti, F. V. 1984a, ApJ 283, 710
Kennel, C. F., Coroniti, F. V. 1984b, ApJ 283, 694
Kobayashi, T., Komori, Y., Yoshida, K., Nishimura, J. 2004, ApJ 601, 340
Lemière, A., for the H.E.S.S. Collaboration, To appear in the Proceedings of the 29th ICRC, Pune (2005)
Leroy, N. et al. 2003, in Proceedings of the 28th International Cosmic Ray Conference (Tsukuba), Vol. 1, 2895 (ArXiv: astro-ph/0307452)
Manchester, R. N., Hobbs, G. B., Teoh, A., & Hobbs, M. 2005, AJ 129, 1993
Mangano, V., Massaro, E., Bocchino, F., Mineo, T., & Cusumano, G. 2005, A&A 436, 917
Nel, H.I. et al. 1996, ApJ 465, 898
Nolan, P. L, Tompkins, W. F., Grenier, I. A., & Michelson, P. F. 2003, ApJ 597, 615
Porquet, D., Decourchelle, A., & Warwick, R. S. 2003, A&A 401, 197
Roberts, M. S. E., Romani, R. W., Kawai, N. 2001, ApJS 133, 451
Sakurai, I., Kawai, N., Torii, K., & Shibata, S. 2001, in ASP Conf. Ser. 251, New Century of X-Ray Astronomy, ed. H. Inoue & H. Kunieda (San Francisco: ASP), 408
Slane, P., Yang, C., Schulz, N. S., Seward, F. D., Hughes, J. P. & Gaensler, B. M. 2000, ApJ 533, L29
Slane, P., Helfand, D. J, van der Swaluw, E., & Murray, S. S 2004, ApJ 616, 403

van der Swaluw, E., & Wu, Y. 2001, ApJ 555, L49
Weisskopf, M. C., et al. 2000, ApJ 536, L81
Zhang L., & Cheng, K. S. 1998, A&A 335, 234

List of Objects

‘HESS J1825–137’ on page 1
‘PSR J1826–1334’ on page 1
‘PSR B1823–13’ on page 1
‘HESS J1825–137’ on page 1
‘G18.0–0.7’ on page 1
‘MSH–15–52’ on page 1
‘HESS J1514–591’ on page 1
‘Vela X’ on page 1
‘HESS J0835–455’ on page 1
‘Kookaburra’ on page 1
‘HESS J1420–607’ on page 1
‘HESS J1418–609’ on page 1
‘3EG J1826–1302’ on page 2
‘LS 5039’ on page 2
‘HESS J1826–148’ on page 2
‘G21.5–0.9’ on page 7
‘3C58’ on page 7
‘G0.9+0.1’ on page 7

[1] Max-Planck-Institut für Kernphysik, P.O. Box 103980, D 69029 Heidelberg, Germany
[2] Yerevan Physics Institute, 2 Alikhanian Brothers St., 375036 Yerevan, Armenia
[3] Centre d’Etude Spatiale des Rayonnements, CNRS/UPS, 9 av. du Colonel Roche, BP 4346, F-31029 Toulouse Cedex 4, France
[4] Universität Hamburg, Institut für Experimentalphysik, Luruper Chaussee 149, D 22761 Hamburg, Germany
[5] Institut für Physik, Humboldt-Universität zu Berlin, Newtonstr. 15, D 12489 Berlin, Germany
[6] LUTH, UMR 8102 du CNRS, Observatoire de Paris, Section de Meudon, F-92195 Meudon Cedex, France
[7] University of Durham, Department of Physics, South Road, Durham DH1 3LE, U.K.
[8] Unit for Space Physics, North-West University, Potchefstroom 2520, South Africa
[9] Laboratoire Leprince-Ringuet, IN2P3/CNRS, Ecole Polytechnique, F-91128 Palaiseau, France
[10] APC, 11 Place Marcelin Berthelot, F-75231 Paris Cedex 05, France UMR 7164 (CNRS, Université Paris VII, CEA, Observatoire de Paris)
[11] Dublin Institute for Advanced Studies, 5 Merrion Square, Dublin 2, Ireland
[12] Landessternwarte, Universität Heidelberg, Königstuhl, D 69117 Heidelberg, Germany
[13] Laboratoire de Physique Théorique et Astroparticules, IN2P3/CNRS, Université Montpellier II, CC 70, Place Eugène Bataillon, F-34095 Montpellier Cedex 5, France
[14] DAPNIA/DSM/CEA, CE Saclay, F-91191 Gif-sur-Yvette, Cedex, France
[15] Laboratoire d’Astrophysique de Grenoble, INSU/CNRS, Université Joseph Fourier, BP 53, F-38041 Grenoble Cedex 9, France
[16] Institut für Astronomie und Astrophysik, Universität Tübingen, Sand 1, D 72076 Tübingen, Germany
[17] Laboratoire de Physique Nucléaire et de Hautes Energies, IN2P3/CNRS, Universités Paris VI & VII, 4 Place Jussieu, F-75252 Paris Cedex 5, France
[18] Institute of Particle and Nuclear Physics, Charles University, V Holesovickach 2, 180 00 Prague 8, Czech Republic
[19] Institut für Theoretische Physik, Lehrstuhl IV: Weltraum und Astrophysik, Ruhr-Universität Bochum, D 44780 Bochum, Germany
[20] University of Namibia, Private Bag 13301, Windhoek, Namibia
[21] Universität Erlangen-Nürnberg, Physikalisches Institut, Erwin-Rommel-Str. 1, D 91058 Erlangen, Germany
[22] European Associated Laboratory for Gamma-Ray Astronomy, jointly supported by CNRS and MPG